RSC Advances

ROYAL SOCIETY OF CHEMISTRY

www.rsc.org/advances

RSC Advances

RSCPublishing

ARTICLE

Fabrication and properties of high-performance chlorine doped graphene quantum dots based photovoltaic detector†

Cite this: DOI: 10.1039/x0xx00000x

Received 00th January 2012,
Accepted 00th January 2012

DOI: 10.1039/x0xx00000x

www.rsc.org/

Jianhong Zhao,[a] Libin Tang,*[b] Jinzhong Xiang,*[a] Rongbin Ji,*[b] Yanbo Hu,[b] Jun Yuan,[b] Jun Zhao,[b] Yunjian Tai,[b] and Yuhua Cai[a]

The functionalized graphene quantum dots (GQDs) based materials play important role in developing high-performance, low-cost, large-area optoelectronic devices. The progress, however, is impeded by the good understanding of physical mechanism for GQDs in these devices. In this paper, chlorine doped GQDs (Cl-GQDs) based photovoltaic photodetectors have been fabricated using solution process, it is found that the presence of Cl-GQDs can obviously enhance the performance of the device. The improved performance by Cl-GQDs based devices have been disclosed by systematical studying the structural, morphological, optical, electrical, electrochemical and photoelectrical properties. The important photovoltaic detectors parameters such as saturation current densities (J_0), barrier heights (Φ_b), built-in potentials (V_{bi}), carrier concentrations (N) and depletion layer widths (W_d) have been calculated and discussed by studying *I-V* and *C-V* characteristics under different illuminations. The frequency dependent capacitance and conductance have also been discussed. The results provide guidance to developing high-performance graphene based optoelectronic devices.

1 Introduction

Graphene quantum dots (GQDs) has been regarded as a kind of new multifunctional materials due to its unique optical, electrical and photoelectric properties. GQDs shows obvious advantages over graphene as far as the modulation of energy-level related properties is concerned. Recently GQDs has been investigated in photovoltaic devices.[1,2] It has been widely reported that graphene plays the carrier transport layer role in the devices because of the outstanding conductivity and shows ultrafast photoresponse and broadband absorption.[3-6] For example, Zhang *et al* fabricated a graphene-polymer nanocomposite membrane, they firstly used it to fabricate mode lock fiber laser. A 700 *fs* pulse width at 1590 nm wavelength has been directly generated from the laser.[7] Zheng *et al* reported the saturable absorption of graphene at microwave frequency band.[8] Compared with graphene, GQDs has more attractive features such as photoluminescence and non-zero bandgap,[9-11] which is tunable by controlling the size and surface modification. Their facile solution processing, quantum confinement effect, bandgap tunability, and multiexciton generation make them particularly attractive as the charge generation layer in photodetectors.[12-14]

GQDs preparation methods include chemical synthesis,[10,15] graphene oxide (GO) reduction,[9,16] carbon nanotubes (CNTs) disintegration transformation,[17] *etc*. The properties of GQDs have been modified by different elements doping, Li *et al* prepared sulphur doped GQDs (S-GQDs) and Cl-GQDs through a facile hydrothermal method, the electronic structures of the GQDs have been tuned by introducing S-related (or Cl-related) energy levels between π and π* of C, leading to efficient and multiple emissions.[18,19] Qu *et al* using urea prepared nitrogen doped GQDs (N-GQDs), resulting in a great improvement in photoluminescence (PL) quantum yield (QY) of GQDs.[20] Vertical heterostructures made with multilayer GQDs sandwiched between graphene sheets by Kim *et al*, achieved high detectivity ($>10^{11}$ cm·Hz$^{1/2}$·W^{-1}) and big responsivity (0.2~0.5 A·W^{-1}) in the broad spectral ranging from ultraviolet (UV) to near infrared (NIR).[12] Tang *et al* reported layered structure N-GQDs possess broadband emission ranging from 300 to >1000 nm, the responsivity of the photodetector is as high as 325 V·W^{-1} under 405 nm laser irradiation.[14]

Compared with graphene photodetector, the response wavelength of GQDs based photodetector is adjustable due to its size dependent energy bandgap. Nowadays, many researchers focus their attention on preparation of GQDs based heterojunction photovoltaic detectors. However, the charge transport properties of GQD-based photoelectric device was rarely reported. Carrier transport mechanism and

photoconductive behaviour of organic heterojunction are different from that of conventional inorganic devices,[21,22] under illumination the excitons are generated in the photoactive layers (*e.g.* P3HT/Cl-GQDs) and dissociated into electrons and holes at the donor/acceptor interfaces. The interface states play an important role in determination of barrier height and other electronic parameters, affecting photovoltaic device performance.[23] Therefore, it is important to make clear the charge transport properties of GQDs based photoelectric devices.

Both quantum confinement (size, edge effect *etc*.) and doping may affect the bandgap of GQDs. In this work, we mainly study the influence of doped chlorine on the properties of GQDs. The bandgap of GQDs measured by cyclic voltammetry in our work is 1.36 eV, similar to the value (0.8-2.508 eV) that reported by the literatures.[24-26] The electrical and photoelectric properties of GQDs based photovoltaic detectors have been investigated by systematic studying the current density-voltage (*J-V*) and the *C-V* characteristics of ITO/PEDOT:PSS/Cl-GQD:P3HT/Al devices under different illuminations. The important electrical and photoelectric parameters such as barrier height (Φ_b), built-in potential (V_{bi}), carrier concentration (N) and depletion layer width (W_d) have been calculated and discussed accordingly.

2 Experimental section

2.1 Materials

All the chemical reagents used in the experiments were purchased without further purification. High-purity reagents (*e.g.* NMP) (99.9%) were purchased from Tianjin FengChuan chemical reagent Technology Co. Ltd., PEDOT:PSS and P3HT were purchased from Sigma-Aldrich.

2.2 Preparation of Cl-GQDs

Cl-GQDs were prepared using a liquid-phase exfoliation method. Degreasing cotton was fully carbonized into carbon fibers (CFs) after heated in air atmosphere at 1000℃ for 30 min. The CFs were ground adequately. 1.0 g CFs was chlorinated with hydrochloric acid (HCl 100 ml, 6 mol·L^{-1}), halogen and oxygen functional groups were introduced on layered structure CFs. Here, HCl plays two roles: One is to provide a Cl doping source; the other is to exfoliate the CFs into small pieces. After that, turbid liquid was washed by distilled water until the pH reached neutral. Then, the chlorinated CFs (0.5 g) was added into 80 mL NMP as solution A. The solution A was treated by ultrasonic dispersion machine for 10 h. The resultant dispersion was centrifuged for 45 minutes at 4000 rpm. After centrifugation, the top clear solution has been collected.

2.3 Fabrication of photovoltaic detectors

The P3HT/Cl-GQDs devices were prepared as follows: P3HT and Cl-GQDs were dissolved in chlorobenzene at a concentration of 15 mg ml^{-1}. The solutions were mixed for 4 h in ultrasonic bath. The mixed solution was filtered with a 0.22 μm polytetrafluoroethylene (PTFE) syringe filter. ITO substrates have been cleaned consecutively with acetone, ethanol and distilled water in ultrasonic bath. After blow-drying, the substrates were cleaned with Ar plasma. PEDOT:PSS solution was first spin-coated on the ITO substrates with a speed of 2000 rpm. After dried at 80℃ for 10 min, the active layers of the photovoltaic devices were deposited with P3HT/ Cl-GQDs solutions at a spinning speed of 2000 rpm. The Al electrode was thermally deposited onto the surface of the active layers in a vacuum chamber (~10^{-4} Pa). The P3HT devices (contrast devices) were prepared using the similar fabrication process but in absence of Cl-GQDs in active layers.

2.4 Characterization

The HRTEM was performed on a JEM-2100 electron microscope operating at 200 kV. The Raman spectrum was recorded at ambient temperature on a Renishaw inVia Raman microscope with an argon-ion laser at an excitation wavelength of 514.5 nm. The FTIR spectra were measured by a Thermo Nicolet Avatar 360 spectrometer using the KBr pellet technique. Optical properties were characterized by UV-Vis, UV-Vis-NIR (U-4100) and fluorescence (Hitachi F-7000) spectrometers. Functional groups on the surface of the Cl-GQDs were verified by XPS (PHI VersaProbe II) using 50W AlKα radiation. The surface morphology and phase image of photovoltaic devices were measured through SEM (FEI Quanta 200) and AFM (SPA-400), respectively.

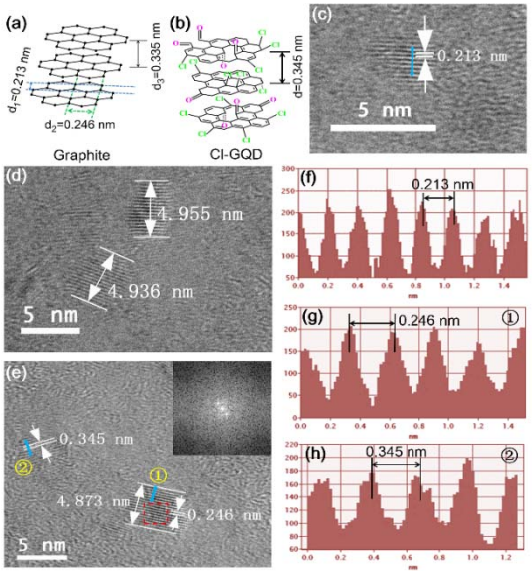

Fig. 1 (a) The basal plane spacing (d_3=0.335 nm) of graphite. (b) The schematic diagram of a Cl-GQD. (c) The HRTEM image of a typical single Cl-GQD, the spacing between the lattice fringe is 0.213 nm. (d) The HRTEM image of Cl-GQDs, the size is about 5 nm. (e) The HRTEM image of Cl-GQDs with the lattice fringes spacings of 0.246 nm and 0.345 nm, inset: the FFT pattern of a selected area (red square) of Cl-GQD. (f), (g), (h) The line profile analyses (blue line) on the Cl-GQDs.

3 Results and discussion

3.1 Characterization of Cl-GQDs

The crystalline structures of graphite and Cl-GQDs[27] are shown in Figure 1(a) and Figure 1(b), respectively. The lattice parameter of 0.213 nm (d_1) corresponds to the $(1\bar{1}0)$ and $(\bar{1}10)$ planes of graphite, and 0.246 nm (d_2) equals to the hexagonal lattice.[28] Moreover, the basal plane spacing is 0.335 nm (d_3).[14,29]

Figure 1(c) is the high-resolution transmission electron microscopy (HRTEM) image of a typical single Cl-GQD with the lattice spacing of 0.213 nm, whose line profile analysis is shown in Figure 1(f). Figure 1(d) is the HRTEM image of Cl-GQDs, the size is about 5 nm. Figure 1(e) shows other Cl-GQDs, similarly, the lattice fringes can be clearly observed, the size is also about 5 nm. In this image, two sets of lattice fringes are observed: 0.246 nm is the in-plane graphene lattice constant, 0.345 nm (d) corresponds to the basal plane spacing of Cl-GQDs. Their line profile analyses are shown in Figure 1(g) and (h), respectively. The plane spacing is slightly larger than that of bulk graphite because the introduced functional group increases the interlayer spacing of Cl-GQDs. The fast Fourier transform (FFT) pattern of the selected area (red square) is shown in the inset of Figure 1(e), two bright points are resulted from the diffraction of $(1\bar{1}0)$ and $(\bar{1}10)$ planes.

Figure 2(a) shows Raman and Fourier transform infrared (FTIR) spectra of the Cl-GQDs. It can be seen from Raman spectrum, there are three dominating vibrational peaks centered at 1340 cm^{-1} (D peak), 1598 cm^{-1} (G peak) and 2692 cm^{-1} (2D peak), respectively. The FTIR spectrum shows that there are four peaks located at 603 cm^{-1}, 804 cm^{-1}, 1050 cm^{-1} and 1089 cm^{-1}, respectively. According to Sadtler Handbook of Infrared Spectra,[30] 1050 cm^{-1} and 1089 cm^{-1} may be the C-Cl vibration peaks of chlorinated aromatic hydrocarbons, while 603 cm^{-1} and 804 cm^{-1} are the C-Cl vibration peaks of chlorinated aliphatic hydrocarbons. This indicates the effectiveness of the Cl doping in Cl-GQDs. As for the dopant concentration, it can be adjusted by tuning HCl concentration within limits. The band at 1619 cm^{-1} is attributed to the stretching vibration of C=C, which is the dominating unit of Cl-GQDs. Another peak at 1724 cm^{-1} may be attributed to C=O stretching. The bending vibration of C-H (1388 cm^{-1}, 881 cm^{-1}), the stretching vibration of C-H (2921 cm^{-1}) and the stretching vibration of O-H (3438 cm^{-1}) [31,32] are also observed in the FTIR spectrum.

X-ray photoelectron spectroscopy (XPS) measurements were carried out to investigate the chemical bonding of the Cl-GQDs. It is worth noting that the pristine degreasing cotton contains no Cl, because the XPS measurements have been carried out in our prior works for Cl-free GQDs which was obtained from the degreasing cotton derived carbon fiber without HCl modification. Figure 2(c) shows the high-resolution C1s XPS spectrum of Cl-GQDs, the measured C1s XPS spectrum is deconvoluted into 4 peaks, which exhibits different types of bonding to C. Figure 2(d) is the Cl2p XPS spectrum, it can be deconvoluted into 4 peaks, *i.e.*, -OCCl (198.2 eV, $Cl2p_{3/2}$), -OC6Cl4O (199.3 eV, $Cl2p_{3/2}$), -C6H4Cl (200.5 eV, $Cl2p_{3/2}$) and -CH2Cl (201.9 eV, $Cl2p_{1/2}$), respectively.[19,33,34] The deference in binding energies for $Cl2p_{1/2}$ and $Cl2p_{3/2}$ is due to the spin-orbit splitting of the Cl2p core level.

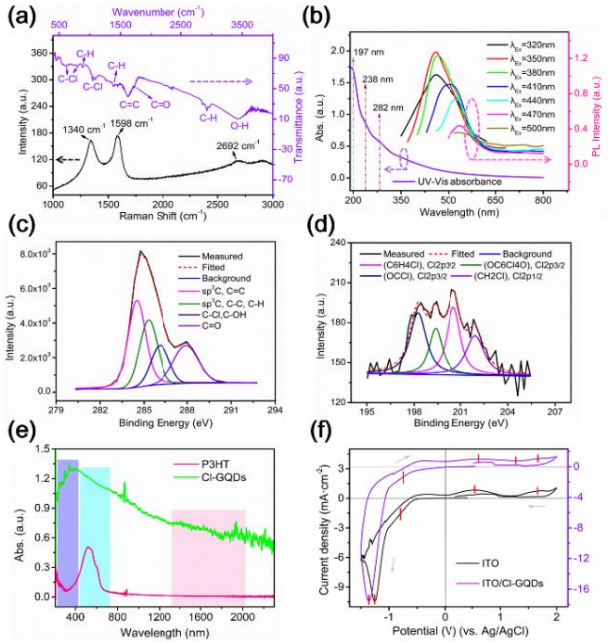

Fig. 2 (a) The Raman and FTIR spectra of Cl-GQDs. (b) The UV-Vis absorption, PL spectra of Cl-GQDs aqueous solution. (c) The C1s XPS spectrum of Cl-GQDs. (d) The Cl2p XPS spectrum of Cl-GQDs. (e) The UV-Vis-NIR absorption spectra of P3HT and Cl-GQDs films. (f) The cyclic voltammetry curve of Cl-GQDs deposited on ITO electrode in 0.1 M Na_2SO_4 with a scan rate of 10 $mV \cdot s^{-1}$.

In order to investigate the optical properties of Cl-GQDs, the UV-Vis absorption and photoluminescence (PL) spectra of Cl-GQDs aqueous solutions were measured, the results are shown in Figure 2(b). Similar to other doped GQDs,[18,35] the PL spectra indicate that the emission peak and the intensity depend on the excitation wavelength (λ_{Ex}). The excitation wavelength ranges from 320 nm to 500 nm with an increase of 30 nm. When, the strongest PL emission peak appears at around 458 nm when the sample excited with λ_{Ex} =350 nm. The origin of the luminescence could be attributed to zigzag sites with the carbene-like triplet ground state.[36] For the UV-Vis absorption spectra, multiple absorption peaks located at 197, 238, and 282 nm are observed. The multiple absorptions can be explained as follows, when the Cl-GQDs irradiated by a certain energy light, the absorbed photons may cause electron transitions between C π and C π^*. Since the effective doping of Cl may introduce additional energy levels, which diversifies the electron transitions.[19] Three types of absorption at 197 nm (6.29 eV), 238 nm (5.20 eV) and 282 nm (4.39 eV) correspond to three electron transition pathways, respectively. This shows the potential applications in light-conversion or optoelectronic devices. The UV-Vis-NIR absorption spectra of the P3HT and Cl-GQDs films coated on quartz plates are shown in Figure 2(e),

which were utilized to determine the optical bandgap of as-prepared materials. For Cl-GQDs solid thin film, three absorption peaks located at 299, 342, and 399 nm which is similar to that of Cl-GQDs aqueous solutions, but with a redshift of about 100 nm. This may be induced by photon reabsorption (Cl-GQDs could be aggregated during film-forming). The redshift has also been reported before and is attributed to the increase in sp^2 content.[13,37] Additionally, the visible and broad NIR absorption bands are highlighted in cyan and pink in Figure 2(e), respectively. The NIR absorption could be attributed to the large conjugated system containing extensive delocalized π electrons in the layered Cl-GQDs.[14] Furthermore, the UV-Vis-NIR absorption spectra of the P3HT films were measured, the noticeable peak located at 520 nm indicate that P3HT mainly absorb visible light. In Figure 2(e), the noise near to 900 nm is caused by the change of light source in spectrometer rather than the signals of samples.

3.2 Electrochemical Measurements

The energy levels of as-prepared Cl-GQDs are evaluated by electrochemical method.[32,38] The oxidation potential and the reduction potential correspond to the valence band edge and the conduction band edge, respectively. The electrochemical measurements were carried out using a CHI627D electrochemical analyser. The cyclic voltammetry (*CV*) curves were measured in 0.1 M Na_2SO_4 solution in a standard three-electrode cell with the Ag/AgCl (3 M KCl) and platinum mesh (PM) as the reference and counter electrodes, respectively. The working electrode was prepared by drop-casting of Cl-GQDs solution onto the indium tin oxide (ITO) electrode. The *CV* curves were recorded from -1.5 V to +2.0 V at a scan rate of 10 $mV \cdot s^{-1}$. The control sample (blank ITO) was measured under the same conditions. The obtained *CV* curves are shown in Figure 2(f). Compared with the control sample, we note that the -1.36 V cathode peak (the reduction of oxygen functionalities) shifts towards more negative potential, while the -0.75 V cathode peak and the 0.61 V anode peak shift towards more positive potential. This hysteresis effect may be due to different surface functional groups of Cl-GQDs and ITO. These *CV* characteristics are similar to those previously reported graphene oxide (GO).[39,40] Thus, from the reduction and oxidation peaks and the proposed equations,[9] the HOMO and LUMO of Cl-GQDs are calculated to be -5.01 eV and -3.65 eV, respectively, the corresponding electrochemical energy gap E_g is 1.36 eV. In addition, an extra oxidation peak at 1.27 V is observed, which may be related to chlorine-containing functional groups.

Furthermore, the oxidation and reduction reactions of Cl-GQDs were directly investigated on Au electrode and PM counter electrodes in N-Methylpyrrolidone (NMP)-based Cl-GQDs solution using ~0.05 M Na_2SO_4 as supporting electrolyte. The measured cyclic voltammetry curve is shown in Figure S1 (ESI†). It can be seen that the *CV* curve exhibits two oxidation peaks located at 0.61 V and 1.36 V, respectively. However, the reduction peak is not obvious, probably due to the difference in solvents.

3.3 Characterization of devices

To explore the applications of Cl-GQDs in optoelectronic fields, P3HT/Cl-GQDs organic heterojunction photovoltaic detectors were fabricated. To improve the charge extraction and transport properties, an interfacial buffer layer (poly(3,4-ethylenedioxythiophene)-poly (styrene sulfonate), POEDOT: PSS) was spin-coated onto ITO. The active layers were prepared by spin-coating a solution of 15 mg mL^{-1} P3HT in chlorobenzene with Cl-GQDs contents of 0, 10 *wt*%. Al was finally vacuum deposited as the top electrode. The detailed fabrications of photovoltaic detectors are described in Experimental section. In our organic heterojunction photovoltaic detector, the donor and acceptor are mixed and deposited as one active layer, the performance of device strongly depends on the morphology of active layer. Atomic Force Microscopy (AFM) topographic images were widely used to measure the morphology of devices.[41,42] Herein, the use of AFM phase image to differentiate the component phase of heterogeneous composites was proposed. Figure 3(a) and (c) are the AFM phase and topographic images of the device using pure P3HT as active layer, respectively. The film is uniform with a root-mean-square (RMS) roughness of 1.09 nm. In the inset of Figure 3(a), a statistical distribution on equivalent disc radius (r_{eq}) is obtained, the average particle size is about 4 nm. The RMS roughness of the film was increased to 1.24 nm when

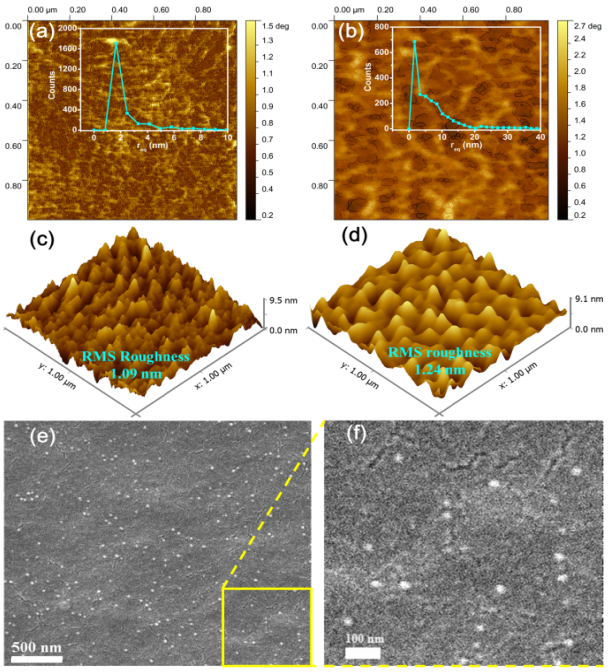

Fig. 3 (a) AFM phase image of P3HT film, inset: size distribution of particles in P3HT film. (b) AFM phase image of P3HT/Cl-GQDs film, inset: size distribution of particles in P3HT/Cl-GQDs film. (c), (d) The AFM topographic images of P3HT and P3HT/Cl-GQDs films with the RMS roughness of 1.09 nm and 1.24 nm, respectively. (e) SEM image of P3HT/Cl-GQDs film. (f) The partial enlarged SEM image of (e).

the film was introduced with 10 *wt*% Cl-GQDs (Figure 3(d)). The phase image (Figure 3(b)) exhibits relatively uniform morphology, which indicates that Cl-GQDs dispersed well in the P3HT matrix. It should be noted that, the statistical distribution on equivalent disc radius (r_{eq}) (Figure 3(b)) shows two sizes: One with average particle size of 4 nm is P3HT, the other with average particle size of 15 nm is Cl-GQDs. The average particle size increases because Cl-GQDs aggregated during film-forming. Comparing the two distributions, a roughly content of Cl-GQDs in the blended film is estimated to be 10%. In addition, the AFM image of Al film was also tested, the obtained RMS roughness is 2.84 nm as shown in Figure S2 (ESI†).

To further investigate the distribution of Cl-GQDs in the active layer, scanning electron microscope (SEM) characterization was conducted, the obtained image is shown in Figure 3(e). It can be seen from Figure 3(e) that Cl-GQDs are uniformly distributed in P3HT polymer matrix. Figure 3(f) is the partial enlarged image of Figure 3(e), it can be clearly seen that the size of Cl-GQDs is about 10~20 nm, the Cl-GQDs content is estimated to be about 10%. The SEM results accord well with that of AFM.

3.4 Current-voltage measurements

The schematic diagram of the Cl-GQD-based photovoltaic detector and its photocurrent generation mechanism are shown in Figure 4(a) and (b), respectively. The photo-generated carriers are produced in the device under illumination through the process of [$h\nu \rightarrow e^- + h^+$], under the built-in potential, photo-generated electron and hole pairs separate and move towards Al and ITO electrodes. Figure 5(a) and (b) show the log *J* vis-à-vis *V* curves of pure P3HT and P3HT/Cl-GQDs devices, respectively (light source: fluorescent lamp, 1.7 mW·cm^{-2}, the same blow). The as-fabricated devices showed good rectification behaviors, suggesting that the charge transport may be described by the thermionic emission theory. The total current density for typical current-voltage characteristics is given by:[43,44]

$$J=J_0\left[\exp(\frac{qV}{\eta k_B T})-1\right] \quad (1)$$

where *V* is the applied voltage, *T* is the absolute temperature, *q* is unit charge, k_B is Boltzmann constant and η is the ideality factor related to the slope. J_0 is the saturation current density obtained by extrapolating the current density from the log-linear plot to *V*=0 and is given by:

$$J_0=A^*T^2\exp(-\frac{q\phi_b}{k_B T}),\ \eta=\frac{q}{k_B T}\left[\frac{\partial(\ln J)}{\partial V}\right]^{-1},\ \Phi_b=q\phi_b=k_B T\ln\frac{A^*T^2}{J_0} \quad (2)$$

and

$$A^*=\frac{4\pi q m^* k_B^2}{h^3} \quad (3)$$

where *A** is the effective Richardson constant, Φ_b is the barrier height, *h* is Plank constant, *m** is the effective electron mass. For P3HT, *m**(1) equals 1.48.[45]

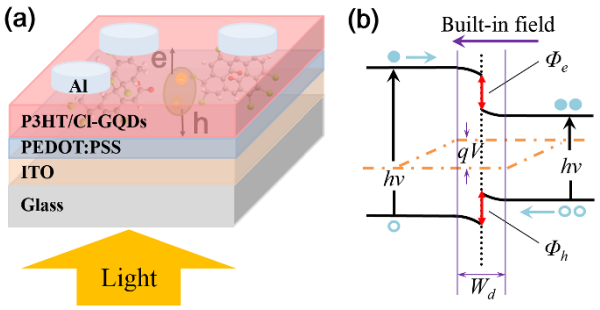

Fig. 4 (a) The schematic diagram of the Cl-GQD-based photovoltaic detector. (b) The schematic illustration for photo-generated carriers. The photo-generated electron (solid circle) and hole (open circle) pairs are separated by the built-in field.

For P3HT/Cl-GQDs, the effective electron mass is achieved according to the equation:

$$m^*(2)=m^*(\text{P3HT})\omega(\text{P3HT})+m^*(\text{Cl-GQDs})\omega(\text{Cl-GQDs}) \quad (4)$$

where ω(P3HT) and ω(Cl-GQDs) are mass fractions for P3HT and Cl-GQDs, respectively, ω(Cl-GQDs)=10% (known from preparation). *m**(Cl-GQDs) ≈ 0.05 (referred from graphite[46] and carbon nanotubes[47]). *m**(2) has been calculated to be 1.34.

When electron transport across the barrier is dominated by thermionic emission as described by equation (1), the logarithmic plots of the *J*-*V* curves display a linear region under forward bias.[44] As seen in Figure 5(a) and (b), the overlying dashed straight-line segments of our fitting allows us to extract J_0 and η for each device. The values of Φ_b under different conditions can be calculated according to equation (2), they are listed in Table 1. Figure 5(f) gives the working mechanism of the Cl-GQD-based photovoltaic detector.

Table 1. The ideality factors, saturation current densities and barrier heights of the P3HT and P3HT/Cl-GQDs bulk heterojunctions.

Device Structure	Working Conditions	η	J_0 (mA·cm^{-2})	Φ_b (eV)
P3HT	dark	1.14	2.12	0.54
	illumination	1.08	4.97	0.38
P3HT/Cl-GQDs	dark	1.76	1.34	0.41
	illumination	1.24	13.48	0.35

3.5 Capacitance-voltage and capacitance-frequency measurements

Generally, *C*-*V* measurements can provide important information on the nature of the semiconductor interface and charge transport. Figure 5(c), (d) and (e) represent the *C*-*V* plots and the variation of $1/C^2$ with applied voltage for two devices at

room temperature under illumination at various frequencies (200 Hz, 1 kHz and 5 kHz), respectively. It can be clearly seen that the capacitance of P3HT/Cl-GQDs device increases more evidently than that P3HT device under the same conditions. This is because Cl-GQDs itself also behaves as a light absorber, which has been proved by the UV-Vis-NIR absorption characterization. The introduction of Cl-GQDs in P3HT matrix may induce more charge. However, all capacitances decrease with increasing frequency. This can be explained as follows, at lower frequencies the interface states can follow the alternating current signal. At high frequencies the interface states remain constant because they cannot follow the alternating signal.[48] In addition, in order to explore the frequency (f) dependent capacitance and conductance (G), the C-f and G-f characteristics for the P3HT and P3HT/Cl-GQDs devices were measured at a serial of voltages ranging from -0.5 to 0.5 V at room temperature, the results are shown in Figure S4 (ESI†).

The C-V relationship under a bias can be expressed as:[49]

$$C^{-2} = \frac{2(V_{bi} - V)}{q\varepsilon_0\varepsilon_r N A^2} \quad (5)$$

where V_{bi} is the built-in potential at zero bias, ε_0 is the permittivity of vacuum, ε_r is the relative permittivity of the material, N is the carrier concentration in the depletion layer and A is the photosensitive area (20 mm^2). The x-intercept is V_{bi}, the carrier concentration N can be calculated from the slope of the linear section of the $1/C^2$ versus V:

$$N = \frac{-2}{q\varepsilon_0\varepsilon_r A^2}\left[\frac{\partial(C^{-2})}{\partial V}\right]^{-1} \quad (6)$$

For P3HT, $\varepsilon_r(1)=3.0$.[50] For Cl-GQDs, ε_r(Cl-GQDs) ≈ 1.88.[51] Similar with the handle of the effective electron mass, the P3HT/Cl-GQDs composite dielectric constant has been calculated as follows,

$$\varepsilon_r(2)=\varepsilon_r(\text{P3HT})\omega(\text{P3HT})+\varepsilon_r(\text{Cl-GQDs})\omega(\text{Cl-GQDs}) \quad (7)$$

The calculated $\varepsilon_r(2)$ is 2.89.

The $1/C^2$-V characteristics of two devices under illumination at 200, 1k, and 5k Hz were shown in Figure 5(c), (d) and (e), respectively. The calculated built in potentials, carrier concentrations were listed in Table 2.

The depletion layer width (W_d) is expressed as:[49]

$$W_d = \left[\frac{2\varepsilon_0\varepsilon_r(V_{bi} - V)}{qN}\right]^{1/2} \quad (8)$$

The depletion layer widths at zero bias voltage were calculated and listed in Table 2 too. As the increase of frequency, the build-in potential and charge carrier concentration decreases while the depletion layer width increases. Under the same conditions, the charge carrier concentration of the P3HT/Cl-GQDs device is 30% higher than that of the P3HT device; As far as the depletion layer width is concerned, however, the W_d of the P3HT/Cl-GQDs device is smaller than that of the P3HT device.

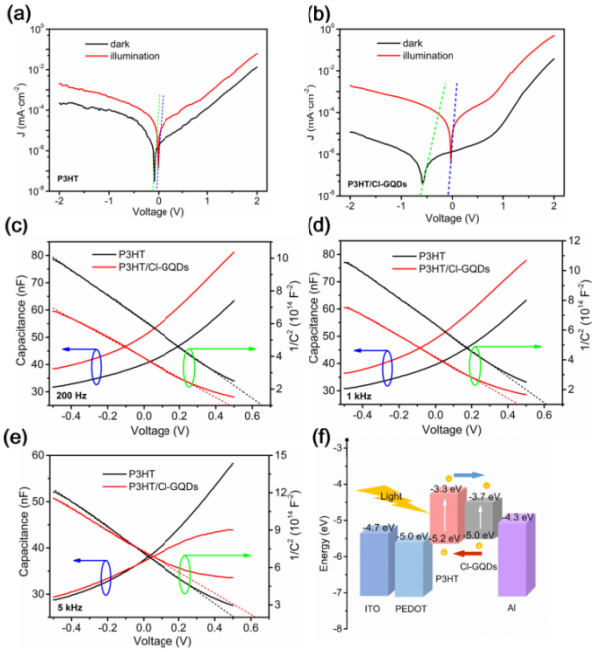

Fig. 5 (a), (b) Logarithmic plots of J vs. V for the P3HT and P3HT/Cl-GQDs photovoltaic detectors under dark and illuminations, respectively. Variation of capacitance with applied voltage and plots of $1/C^2$ *vs.* V characteristics for P3HT and P3HT/Cl-GQDs devices under illumination at various frequencies: (c) 200 Hz, (d) 1 kHz, (e) 5 kHz, respectively. (f) The schematic illustration of the working mechanism of the Cl-GQD-based photovoltaic detector.

Table 2. The built-in potential, carrier concentration and depletion layer width of the P3HT and P3HT/Cl-GQDs bulk heterojunctions at various frequencies.

Device Structure	V_{bi} (V)			N (10^{18} cm^{-3})			W_d (nm) (V=0)		
	200 Hz	1 kHz	5 kHz	200 Hz	1 kHz	5 kHz	200 Hz	1 kHz	5 kHz
P3HT	0.78	0.73	0.70	1.50	1.34	1.15	13.13	13.44	14.21
P3HT/Cl-GQDs	0.64	0.60	0.86	2.01	1.75	1.44	10.09	10.47	13.81

4 Conclusions

The Cl-GQDs based photovoltaic photodetectors were fabricated, the presence of Cl-GQDs in the photoactive layer may obviously enhance the photoresponse of the device. The device is stable, the *J-V* curve remains unchanged after several measurements, the device remains no damage under the light power density up to 165 mW cm^{-2}. The distribution and morphology of Cl-GQDs in P3HT matrix have been investigated by AFM and SEM. The physical mechanism for the function of Cl-GQDs has been disclosed. The improved performance by Cl-GQDs has been uncovered after systematic studying the optical, electrical, electrochemical, photoelectrical properties of the devices. The important device parameters such as saturation current densities, barrier heights, built-in potentials, carrier concentrations and depletion layers widths have been discussed after detailedly studying *I-V*, *C-V* and *C-f* characteristics. The obtained results shown that the carrier concentrations increase by 30% in the presence of Cl-GQDs (~ 10% weight ratio), the depletion layer width decreases compared to Cl-GQDs free devices. The present study may help us to design and fabricate high-performance graphene based optoelectronic devices.

Acknowledgements

This work was supported by National Natural Science Foundation of China (No. 61106098, 51201150), the Key Project of Applied Basic Research of Yunnan Province, China (No. 2012FA003).

Notes and references

[a] *School of Physical Science and Technology, Yunnan University, Kunming, 650091, P. R. China. Email: jzhxiang@ynu.edu.cn*
[b] *Kunming Institute of Physics, Kunming, 650223, P. R. China. Email: scitang@163.com, jirongbin@gmail.com*

† Electronic Supplementary Information (ESI) available: Electrochemistry measurement for *CV* of Cl-GQDs, AFM images, *C-V* curves under high frequencies, *C-f* and *G-f* characteristics. See DOI: 10.1039/b000000x/

1. F. J. Lim, K. Ananthanarayanan, J. Luther and G. W. Ho, *J. Mater. Chem.*, 2012, **22**, 25057-25064.
2. J. H. Lee, J. H. Shin, J. Y. Song, W. F. Wang, R. Schlaf, K. J. Kim and Y. Yi, *J. Phys. Chem. C*, 2012, **116**, 26342-26348.
3. F. Xia, T. Mueller, Y. M. Lin, A. Valdes-Garcia and P. Avouris, *Nat. Nanotechnol.*, 2009, **4**, 839-843.
4. V. Patil, A. Capone, S. Strauf and E. H. Yang, *Sci. Rep.*, 2013, **3**, 2791.
5. B. Y. Zhang, T. Liu, B. Meng, X. Li, G. Liang, X. Hu and Q. J. Wang, *Nat. Commun.*, 2013, **4**, 1811.
6. C.-H. Liu, Y.-C. Chang, T. B. Norris and Z. Zhong, *Nat. Nanotechnol.*, 2014, **9**, 273-278.
7. H. Zhang, Q. Bao, D. Tang, L. Zhao and K. Loh, *Appl. Phys. Lett.*, 2009, **95**, 141103.
8. Z. W. Zheng, C. J. Zhao, S. B. Lu, Y. Chen, Y. Li, H. Zhang and S. C. Wen, *Opt. Express*, 2012, **20**, 23201-23214.
9. V. Gupta, N. Chaudhary, R. Srivastava, G. D. Sharma, R. Bhardwaj and S. Chand, *J. Am. Chem. Soc.*, 2011, **133**, 9960-9963.
10. L. B. Tang, R. B. Ji, X. M. Li, K. S. Teng and S. P. Lau, *Part. Part. Syst. Char.*, 2013, **30**, 523-531.
11. R. Sekiya, Y. Uemura, H. Murakami and T. Haino, *Angewandte Chemie*, 2014, **53**, 5619-5623.
12. C. O. Kim, S. W. Hwang, S. Kim, D. H. Shin, S. S. Kang, J. M. Kim, C. W. Jang, J. H. Kim, K. W. Lee, S. H. Choi and E. Hwang, *Sci. Rep.*, 2014, **4**, 5603.
13. S. K. Lai, L. Tang, Y. Y. Hui, C. M. Luk and S. P. Lau, *J. Mater. Chem. C*, 2014, **2**, 6971-6977.
14. L. B. Tang, R. B. Ji, X. M. Li, G. X. Bai, C. P. Liu, J. H. Hao, J. Y. Lin, H. X. Jiang, K. S. Teng, Z. B. Yang and S. P. Lau, *ACS Nano*, 2014, **8**, 6312-6320.
15. M. L. Mueller, X. Yan, J. A. McGuire and L.-s. Li, *Nano Lett.*, 2010, **10**, 2679-2682.
16. D. Pan, J. Zhang, Z. Li and M. Wu, *Adv. Mater.*, 2010, **22**, 734-738.
17. D. B. Shinde and V. K. Pillai, *Chem.-Eur. J.*, 2012, **18**, 12522-12528.
18. X. M. Li, S. P. Lau, L. B. Tang, R. B. Ji and P. Z. Yang, *Nanoscale*, 2014, **6**, 5323-5328.
19. X. Li, S. P. Lau, L. Tang, R. Ji and P. Yang, *J. Mater. Chem. C*, 2013, **1**, 7308.
20. D. Qu, M. Zheng, L. Zhang, H. Zhao, Z. Xie, X. Jing, R. E. Haddad, H. Fan and Z. Sun, *Sci. Rep.*, 2014, **4**, 5294.
21. Y.-F. Lao, A. G. U. Perera, L. H. Li, S. P. Khanna, E. H. Linfield and H. C. Liu, *Nat. Photonics* 2014, **8**, 412-418.
22. S. Hussain, C. Cao, W. S. Khan, G. Nabi, Z. Usman, A. Majid, T. Alharbi, Z. Ali, F. K. Butt, M. Tahir, M. Tanveer and F. Idress, *Mater. Sci. Semicond. Process.*, 2014, **25**, 181-185.
23. S. Zeyrek, E. Acaroğlu, Ş. Altındal, S. Birdoğan and M. M. Bülbül, *Curr. Appl Phys.* , 2013, **13**, 1225-1230.
24. J. Lu, P. S. Yeo, C. K. Gan, P. Wu and K. P. Loh, *Nat. Nanotechnol.*, 2011, **6**, 247-252.
25. S. H. Jin, D. H. Kim, G. H. Jun, S. H. Hong and S. Jeon, *ACS Nano*, 2012, **7**, 1239-1245.
26. G. Eda, Y. Y. Lin, C. Mattevi, H. Yamaguchi, H. A. Chen, I. S. Chen, C. W. Chen and M. Chhowalla, *Adv. Mater.*, 2010, **22**, 505-509.
27. J. Zhao, L. Tang, J. Xiang, R. Ji, J. Yuan, J. Zhao, R. Yu, Y. Tai and L. Song, *Appl. Phys. Lett.*, 2014, **105**, 111116.
28. L. B. Biedermann, M. L. Bolen, M. A. Capano, D. Zemlyanov and R. G. Reifenberger, *Phys. Rev. B*, 2009, **79**, 125411.
29. J. Slonczewski and P. Weiss, *Phys. Rev.*, 1958, **109**, 272.
30. W. H. S. Sadtler, in *Bio-Rad Laboratories, Inc., Informatics Division*, 1978.
31. W. Zhang, D. Dai, X. Chen, X. Guo and J. Fan, *Appl. Phys. Lett.*, 2014, **104**, 091902.
32. D. Yu, Y. Yang, M. Durstock, J.-B. Baek and L. Dai, *ACS Nano*, 2010, **4**, 5633-5640.
33. J. Y. Kim, W. H. Lee, J. W. Suk, J. R. Potts, H. Chou, I. N. Kholmanov, R. D. Piner, J. Lee, D. Akinwande and R. S. Ruoff, *Adv. Mater.*, 2013, **25**, 2308-2313.
34. The NIST XPS Online, http://srdata.nist.gov/xps/EngElmSrchQuery.aspx?EType=PE&CSOpt=Retri_ex_dat&Elm=Cl, (accessed September 15, 2012).
35. L. B. Tang, R. B. Ji, X. M. Li, K. S. Teng and S. P. Lau, *J. Mater. Chem. C*, 2013, **1**, 4908-4915.
36. L. R. Radovic and B. Bockrath, *J. Am. Chem. Soc.*, 2005, **127**, 5917-5927.
37. Q. Shou, J. Cheng, L. Zhang, B. J. Nelson and X. Zhang, *J. Solid State Chem.*, 2012, **185**, 191-197.
38. J. Tang, K. W. Kemp, S. Hoogland, K. S. Jeong, H. Liu, L. Levina, M. Furukawa, X. Wang, R. Debnath, D. Cha, K. W. Chou, A. Fischer, A. Amassian, J. B. Asbury and E. H. Sargent, *Nat. Mater.*, 2011, **10**, 765-771.
39. Y. Shao, J. Wang, M. Engelhard, C. Wang and Y. Lin, *J. Mater. Chem.*, 2010, **20**, 743.
40. A. Y. S. Eng and M. Pumera, *Electrochem. Commun.*, 2014, **43**, 87-90.
41. A. Tamanai, S. Beck and A. Pucci, *Displays*, 2013, **34**, 399-405.
42. L. Scudiero, H. Y. Wei and H. Eilers, *ACS Appl. Mat. Interfaces* 2009, **1**, 2721-2728.
43. S. M. Sze and K. K. Ng, *Physics of Semiconductor Devices*, John Wiley & Sons, Inc., Hoboken, New Jersey, Canada, third edn.,

2007.
44. S. Tongay, M. Lemaitre, X. Miao, B. Gila, B. R. Appleton and A. F. Hebard, *Physical Review X*, 2012, **2**, 011002.
45. X.-H. Xie, W. Shen, R.-X. He and M. Li, *Bull. Korean Chem. Soc.*, 2013, **34**, 2995-3004.
46. P. Wallace, *Phys. Rev.*, 1947, **71**, 622-634.
47. D. Shah, N. A. Bruque, K. Alam, R. K. Lake and R. R. Pandey, *J. Comput. Electron.* , 2007, **6**, 395-400.
48. V. Rajagopal Reddy, V. Janardhanam, J.-W. Ju, H.-J. Yun and C.-J. Choi, *Solid State Commun.*, 2014, **179**, 34-38.
49. M. Ramar, C. K. Suman, R. Manimozhi, R. Ahamad and R. Srivastava, *RSC Adv.*, 2014, **4**, 32651-32657.
50. G. Garcia-Belmonte, A. Munar, E. M. Barea, J. Bisquert, I. Ugarte and R. Pacios, *Org. Electron.*, 2008, **9**, 847-851.
51. K. Uchida and A. Oshiyama, *Phys. Rev. B*, 2009, **79**, 235444.

